

# High-Pressure Study of the Methylsulfate and Tosylate Imidazolium Ionic Liquids

Santiago Aparicio,\* Rafael Alcalde, Begona García, and José M. Leal\*

Departamento de Química, Universidad de Burgos, 09001 Burgos, Spain

Received: January 13, 2009; Revised Manuscript Received: February 27, 2009

The considerable interest aroused in recent years by the unique properties and industrial applications of ionic liquids has given rise to the need for a detailed statement of the linkage between their molecular features and the observed macroscopic behavior. A combined experimental/computational approach to the study of ionic liquids is submitted here and applied to the relevant, nonhalogenated ionic liquids 1,3-dimethylimidazolium methylsulfate and 1-ethyl-3-methylimidazolium tosylate. To establish a reliable equation of state pertinent to these fluids, density data over wide pressure (0.1–60 MPa) and temperature (318.15–428.15 K) ranges, along with high pressure (1–70 MPa) viscosities and other selected ambient pressure properties were measured to assemble sufficient experimental information for the seek of predictive models for process design. A computational method based on ab initio and classical molecular dynamics yielded a deal of structural information, borne out by the experimental readings. Likewise, the predictive ability of the force field applied in molecular dynamics simulations was faced with the measured properties. The pictorial description of the selected ionic liquids reached this way may become widespread to other relevant examples in order to infer valuable structure/property relationships.

## Introduction

The increasingly severe environmental controls that stem from the social demand for a sustainable development have prompted the industrial activity to evolve into cleaner, safer, and more efficient processes.<sup>1</sup> In a green chemistry context, the design of processes should be capable of retaining the economic viability of technological progress while being respectful toward the environment, reducing pollution to a minimum.<sup>2</sup> Such a challenge requires new tools. Among the different options developed so far, ionic liquids (ILs) have proved to be promising alternatives to organic solvents<sup>3</sup> and efficient reaction media in synthesis, separation, electrochemistry, and engineering fluids.<sup>4–7</sup> The amazing versatility of this sort of fluids may enable selective anion/cation combinations such that suitable ILs endowed with specific properties can be tailored.<sup>8</sup> That is the origin of the term designer solvents,<sup>9</sup> which has led to ILs with favorable profile<sup>10</sup> giving way to a new chemistry based on precise structure/property relationships.<sup>11,12</sup> In practice, due to economical and time-consuming constraints, the large number of potential anion/cation permutations makes unfeasible the data supply over wide pressure/temperature ranges,<sup>13</sup> which could hinder the development of this promising technology. Hence, ILs must be designed carefully.

The wide slate of candidates differ by their environmental and toxicological features.<sup>14</sup> Even though ILs are nonvolatile fluids, this feature does not suffice of itself to term all of them as green solvents. For instance, halogenated ILs that release hydrofluoric or hydrochloric acids are environmentally unfavorable,<sup>15</sup> as are those containing the toxicologically unfriendly  $\text{PF}_6^-$  anion.<sup>16</sup> Therefore, the study of ILs should be tackled systematically considering (i) selected families of fluids, (ii) properties measured over wide ranges of pressure/temperature, and (iii) theoretical studies leading to molecular information and accurate predictive models (Figure 1). In this work, the

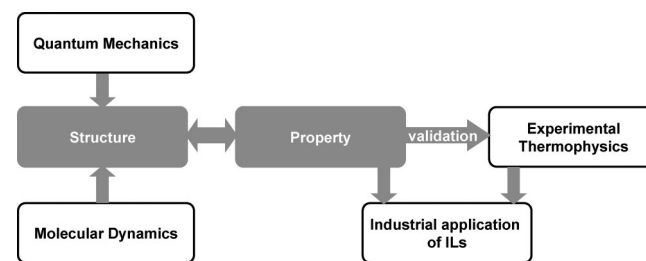


**Figure 1.** Scheme of the proposed experimental/computational approach to the study of ionic liquids.

nonhalogenated ILs 1,3-dimethylimidazolium methylsulfate, [DMIM]MS, and 1-ethyl-3-methylimidazolium tosylate, [EMIM]-TOS have been studied. These compounds can be synthesized easily from inexpensive materials.<sup>17</sup> Alkylimidazolium ILs become less toxic the shorter the alkyl chain.<sup>14,18</sup> Imidazolium ILs can be prepared to a large scale using simple precursors.<sup>19</sup> The low-toxic,<sup>20</sup> biodegradable<sup>21</sup> alkylsulfate anions are seen as sound alternatives to halogenated anions.<sup>22</sup> The tosylate anion also displays favorable profile.<sup>20</sup>

Therefore, this work pursues (a) to analyze the anion effect over wide ranges of pressure/temperature, (b) to bring in molecular information from the anion/cation features, and (c) to infer the prediction ability of theoretical models. A number of thermophysical properties were studied according to their applications and the molecular information released: (1) Density as a function of pressure and temperature (PVT behavior); despite its key role and the thermodynamic information conveyed, only scarce studies have been carried out.<sup>23</sup> (2) Viscosity as a function of pressure and temperature, it bears a close relation with diffusion and intermolecular forces; being an essential property in operations such as stirring, mixing, or pumping, data on the pressure effect are scarce.<sup>24</sup> (3) Isobaric heat capacity, a relevant property for heat transfer and design of operations;<sup>3</sup> as the PVT data allow calculations at other pressures, it was measured as a function of temperature only.

\* To whom correspondence should be addressed. E-mail: (S.A.) [sapar@ubu.es](mailto:sapar@ubu.es); (J.M.L.) [jmleal@ubu.es](mailto:jmleal@ubu.es).

(4) Conductivity, a property that provides information on ions mobility and anion/cation interactions.<sup>25</sup> The theoretical study was carried out from two complementary views: (i) density functional theory (DFT) study of the anion/cation interaction and short-range effects on fluid structure, and (ii) classical molecular dynamics (MD) simulations of the liquid structure to predict macroscopic properties; the comparison with measured properties allows us to establish relations between fluid's structure, intermolecular forces, and macroscopic behavior.

## Materials and Methods

**Ionic Liquids Samples.** [DMIM]MS (99.0% purity) and [EMIM]TOS (99.4% purity) were purchased from Fluka. Despite its high melting temperature (49.75 °C from Domanska et al.,<sup>26</sup> 53 °C from Strehmel<sup>17</sup>), at 5 °C [EMIM]TOS remains as a subcooled melt for a long time; once melted, it is a faintly yellow viscous fluid. [DMIM]MS (melting point 43 °C)<sup>17</sup> also behaves as a slightly yellow subcooled melt, and at -20 °C it forms a liquid for a long time. The presence of color in both liquids reveals impurities,<sup>19</sup> almost ubiquitous in commercial ILs. Although such impurities might be a serious pitfall in electrochemistry and catalysis, their physical properties remain unaffected; therefore, procedures for color removal were ruled out. Conversely, as water has a relevant effect on the physical properties, the water content was reduced to a minimum by drying the commercial sample at 80 °C for several hours under vacuum.<sup>28</sup> The water content, evaluated by Karl Fischer Coulometry titration, was 330 ppm for [EMIM]TOS and 200 ppm for [DMIM]MS.

**PVT Behavior.** The PVT apparatus is installed around a high-pressure vibrating tube density meter.<sup>29</sup> The cell temperature was controlled by a Julabo F32 bath and measured to ±0.01 K by a Pt100 sensor located in the measuring cell connected to an ASL-F250 unit. The sample pressure was controlled to ±5 × 10<sup>-3</sup> MPa by a Ruska 7615 Digital Pressure controller and measured with a pressure sensor to ±0.01 MPa. The pressure transducer and the thermometer were calibrated using fully traceable procedures; a 14-parameter equation was used with *n*-hexane (Fluka, 99.9%) and water (Millipore, 18.2 mΩ cm resistivity) as reference fluids.<sup>30</sup> The viscosity effect on the sample density was below the uncertainty limit (±1 × 10<sup>-4</sup> g cm<sup>-3</sup>),<sup>22b</sup> thus the raw data were used without viscosity correction. From the fitting of the 10-parameter TRIDEN equation to the density readings<sup>31</sup> the derived properties isobaric thermal expansivity ( $\alpha_p$ ), isothermal compressibility, ( $k_T$ ), and internal pressure ( $P_i$ ) were calculated (Tables S1–S3, Supporting Information).<sup>22b</sup>

**High-Pressure Viscosities.** Viscosities ( $\eta$ ), were measured using an electromagnetic VINCI Tech. EV1000 viscometer; the uncertainty of the reported absolute viscosity data at high pressures was estimated to be ±2%. The system was set up around a measuring sample chamber connected on top and bottom to system lines that enable the liquid sample be either admitted or expelled. A stainless steel piston inside a sensor is electromagnetically driven back and forth at a constant force using two magnetic coils. The motion of the piston is impeded by the viscosity of the fluid. Therefore, the piston's two-way travel time can be analyzed and converted into absolute viscosity reading, which measures the resistance of the fluid to flow. To expand the overall viscosity span, pistons of different size were used pursuant to the viscosity range to be covered, thus improving the uncertainty. The sample heating was provided and controlled by an external Julabo F32 recirculating bath and measured (±0.01 K) by a built-in platinum resistance probe.

The sample pressure was controlled by a VINCI BSP65 syringe pump with the cell pressure being measured to ±0.01 MPa with a pressure transducer. The apparatus was calibrated using certified oils provided by the manufacturer, and the temperature and pressure sensors were calibrated using traceable procedures. The Tait equation was fitted to the viscosity data-pairs over the whole pressure/temperature ranges<sup>32</sup>

$$\eta = A \exp\left(\frac{B}{T - C}\right) \exp\left(D \ln\left(\frac{P + E}{0.1 \text{ MPa} + E}\right)\right) \quad (1)$$

the fitting parameters  $A$ ,  $B$ ,  $C$ , and  $D$  being evaluated by least-squares, and  $E$  being defined as

$$E = E_0 + E_1 T + E_2 T^2 \quad (2)$$

The pressure viscosity ( $\alpha_\eta$ ) and temperature viscosity ( $\beta_\eta$ ) coefficients, calculated according to eqs 3 and 4, are reported in Tables S4–S6 (Supporting Information)

$$\alpha_\eta = \left(\frac{1}{\eta}\right) \left(\frac{\partial \eta}{\partial P}\right)_T = \frac{D}{P + E} \quad (3)$$

$$\beta_\eta = -\left(\frac{1}{\eta}\right) \left(\frac{\partial \eta}{\partial T}\right)_P = \eta \left( \frac{-B}{(T - C)^2} \right) + \eta D(E_1 + 2E_2 T) \frac{0.1 \text{ MPa} - P}{(0.1 \text{ MPa} + E)(P + E)} \quad (4)$$

**Isobaric Heat Capacity.** This property was measured with a Setaram micro DSC III calorimeter.<sup>33</sup> Measurements were carried out according to the continuous scanning method,<sup>34</sup> using toluene (Fluka, >99.8%) as reference material and butan-1-ol (Aldrich, >99.5%) as a calibration liquid.<sup>35</sup> The signal is proportional to the volume heat capacity; the measured densities were used to obtain molar heat capacities (±0.01 J mol<sup>-1</sup> K<sup>-1</sup>), the temperature being controlled to ±0.01 K by a peltier. Measurements were carried out at atmospheric pressure (0.1 MPa) and calculated at other pressures using thermodynamic relations.<sup>22b</sup>

**Conductivity Measurements.** Measurements (1%) were carried out using a Radiometer CDM210 conductivity meter, previously calibrated using KCl standard solutions. Electrode and samples were placed in a sealed glass cell, immersed in a Julabo F32 bath. The sample temperature (±0.01 K) was measured with a platinum resistance thermometer. The results are reported in Table S7 (Supporting Information).

**Quantum Calculations.** Quantum calculations were carried out with the Gaussian 03 package<sup>36</sup> according to the DFT, using the Becke gradient corrected exchange functional<sup>37</sup> and Lee–Yang–Parr correlation functional<sup>38</sup> with the three parameters (B3LYP)<sup>39</sup> method. To properly describe the electrons far from and close to the nuclei, use of large and flexible basis sets is advisable, here 6-311++g\*\* was used. For a proper fitting of the electrostatic potential, the atomic charges were calculated according to the Merz–Singh–Kollman (MK) scheme.<sup>40,41</sup> The ion-pair interaction energy,  $\Delta E$ , was calculated as the difference between the pair and the sum of the separated ions energies at the same theoretical level, with basis set superposition error (BSSE) corrected using the counterpoise procedure.<sup>42</sup>

**MD Simulations.** Classical MD simulations were carried out using the TINKER molecular modeling package.<sup>43</sup> All the simulations were performed in the NPT ensemble; the

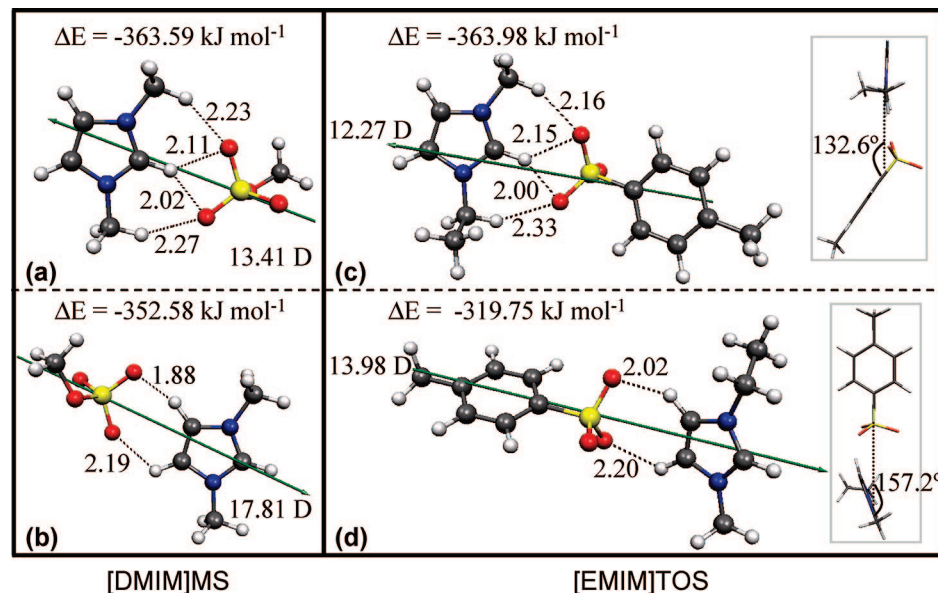


**Figure 2.** Optimized gas phase structures (B3LYP/6-311++g\*\*) of studied ion pairs.  $\Delta E$  = counterpoise corrected interaction energy. Color code: (dark gray) carbon, (light gray) hydrogen, (red) oxygen, and (yellow) sulfur. In panels (c) and (d), a top view shows the angles between rings. Green arrow = calculated dipole moment. Distance in angstroms.

Nosé–Hoover method<sup>44</sup> was used to control the temperature and pressure of the simulation system. The motion equations were solved using the Verlet Leapfrog integration algorithm.<sup>45</sup> The molecular geometries were restrained according to the shake algorithm.<sup>46</sup> Long-range electrostatic interactions were treated with the smooth particle mesh Ewald method.<sup>47</sup> The simulated system consists of cubic boxes with 250 ions (125 anions, 125 cations) to which periodic boundary conditions were applied in all three directions. The initial liquid box size was established according to the experimental densities. The simulations were performed using an  $L/2$  Å cutoff radius for the nonbonded interactions with  $L$  being the box side. Initial boxes were generated with the PACKMOL program<sup>48a</sup> using the BOX-QUACAN<sup>48b</sup> local-minimization method to obtain adequate starting configurations. The boxes were minimized using the MINIMIZE program, TINKER package, to a 0.01 kcal mol<sup>-1</sup> Å<sup>-1</sup> rms gradient, then several heating and quenching steps in the NVT ensemble were performed up to 500 K, and a 100 ps NVT equilibration simulation was run at the set temperature; finally, from the output NVT configuration, a 5 ns (time step 1 fs) was run in the NPT ensemble at the set temperature and pressure from which the first 1 ns was used to ensure equilibration (checked to constant energy) and the remaining 4 ns for data collection. The ILs were described according to the so-called optimized potential for liquid simulations (all atom version) OPLS-AA.<sup>49</sup> MK charges obtained through B3LYP/6-311++g\*\* calculations were used in the simulations.

## Results and Discussion

**DFT Ion-Pair Energy and Structure.** Figure 2 displays the relevant structure and energy data of the studied ion pairs. Two main imidazolium ring/anion interacting positions more likely: (i) position 1 (namely front) through the CH group placed between the two nitrogens, and (ii) position 2 (namely back) through the two CH groups, opposite to position 1. Both positions yield large stabilization energy. Although position 1 (Figure 2a,c) is preferred for both [DMIM]MS and [EMIM]TOS, the additional stabilization energy in position 2 (Figure 2b,d) is not very large, specially for [DMIM]MS, 11.0 kJ mol<sup>-1</sup>. The calculated electronic density surface for the [EMIM]<sup>+</sup> cation

projected onto three planes is shown in Figure 3. The  $z$ -projection shows only a slight difference between positions 1 and 2 (which, in turn, would justify the subtle preference for position 1). The electron depletion in position 1 becomes slightly larger than in position 2 (green contour in position 2), thus position 1 should display a slightly larger electron acceptor ability (more acidic),<sup>50</sup> and interaction with anions through this site should prevail. The  $x$ -projection shows electron depletion in the imidazolium ring, and thus the in-plane interaction with the anion would be preferred to interaction from either top or bottom.

The anion/cation effects leading to the ion pairs depicted in Figure 2 are electrostatic and H-bonding. The calculated C–H···O distance for positions 1 and 2 (below the H-bond distance range) and the angles sketched by the three atoms (greater than 90°) correspond to strong H-bonding interactions.<sup>51</sup> Therefore, the C–H distance should rise from the isolated cation to the remarkable ion pair, due to the weakening of the C–H bond, and thus the stretching vibrational frequency should shift to red (Table 1). In both ion pairs the results indicate a soft lengthening of the C–H bond in position 1 with a similar red shift for the stretching frequency, and a remarkable increase of the S–O length. For [DMIM]MS, the data reveal two unequal H-bonds in position 2. The shorter bond (Figure 2b) is characterized by a notable rise in the C–H length and a rather pronounced shift to red; instead, the C–H length for the longer one is almost unaffected by ion-pair formation, even showing a slight blue shift of the stretching frequency. Thus, H-bond in position 1 evolves toward a strong bond together with a weaker one with the second CH group. Similar results are deduced in position 2 for [EMIM]TOS, though the effect is less perceptible. The increase in the S–O bond length upon ion-pair formation bears out the observed behavior. Charge transfer is another remarkable outcome.<sup>52</sup> Using MK charges, a 0.113 charge transfer is deduced for [DMIM]MS in position 1 and 0.085 in position 2; for [EMIM]TOS, 0.103 in position 1 and 0.078 in position 2. Hence, position 1 favors a more effective anion/cation transfer, though the difference with position 2 is not too large. This effect is the same order as that reported for other

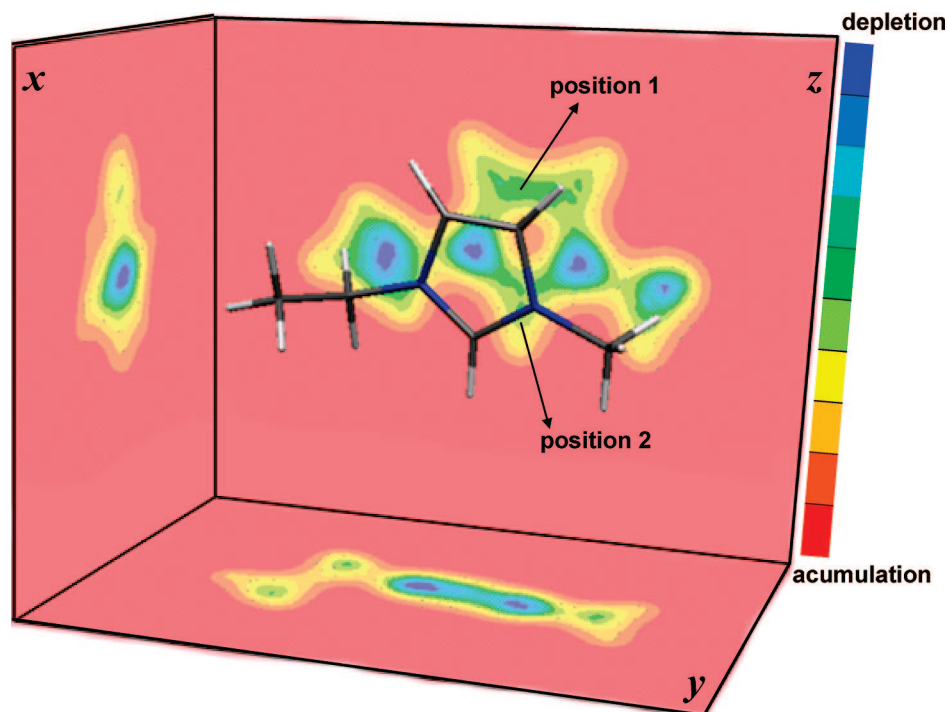


**Figure 3.** Projections of the electronic density surface for  $[\text{EMIM}]^+$  calculated at B3LYP/6-311++g\*\* level.

**TABLE 1: B3LYP/6-311++g\*\* Calculated Bond Distance,  $r$ , and Vibrational Frequency for Ion Pairs<sup>a</sup>**

		atom numbering	$C-H$	$r(C-H)/\text{\AA}$	$\nu(C-H)/\text{cm}^{-1}$	atom numbering	$S-O$	$r(S-O)/\text{\AA}$
$[\text{DMIM}]MS$	position 1	D4-D8		1.083 (+0.005)	3214.7 (-70.8)	M6-M7 M6-M8		1.495 (+0.015)
	position 2	D1-D6		1.093 (+0.015)	3045.0 (-232.4)	M6-M7		1.495 (+0.015)
		D2-D7		1.078 (+0.000)	3283.0 (+5.6)	M6-M8		1.478 (-0.002)
$[\text{EMIM}]TOS$	position 1	E4-E8		1.084 (+0.006)	3191.1 (-93.2)	M10-M8 M10-M9		1.504 (+0.019)
	position 2	E1-E6		1.086 (+0.008)	3153.2 (-123.8)	M10-M8		1.499 (+0.013)
		E2-E7		1.080 (+0.002)	3256.3 (-20.7)	M10-M9		1.496 (+0.010)

<sup>a</sup> Atom numbering as in Figure I (Supporting Information). Parenthesized values: difference between the property in the ion-pair and the property in the isolated ion.

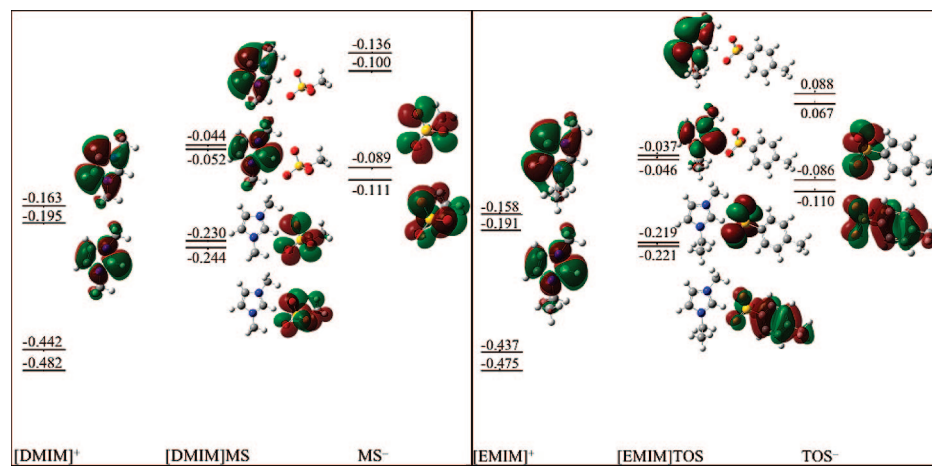


**Figure 4.** Frontier molecular orbitals for cations, anions, and ion pairs in  $[\text{DMIM}]MS$  and  $[\text{EMIM}]TOS$ , calculated at B3LYP/6-311++g\*\* level. From bottom to top: HOMO-1, HOMO, LUMO, and LUMO+1. Figures show a.u. energy for each molecular orbital. Isosurface calculated at 0.02. For cations (electron acceptor) isosurfaces are reported only for LUMO and LUMO+1; for anions (electron donor) isosurfaces are given for HOMO-1 and HOMO; for pairs HOMO-1, HOMO, LUMO, and LUMO+1 isosurfaces are given bottom to top.

imidazolium ILs.<sup>52</sup> The less effective transfer from the TOS anion can be set down to the delocalization through the aromatic ring.

Figure 4 displays the frontier orbitals calculated for isolated ions and ion-pairs interacting through position 1. The energy difference between the donor (anion) highest occupied molecular orbital (HOMO) and acceptor (cation) lowest unoccupied

molecular orbital (LUMO) orbitals is 2.9 eV for both ILs, a figure well below the 6 eV value regarded as the energy gap for an effective overlapping.<sup>53</sup> Shape and phase analyses show that none of the ILs meet the required in-phase HOMO-LUMO overlapping condition. As expected for five-membered rings,  $[\text{DMIM}]^+$  and  $[\text{EMIM}]^+$  bear  $\pi$  LUMO orbitals. The shape and phase of the HOMO and HOMO-1 orbitals in  $MS^-$  hinder the

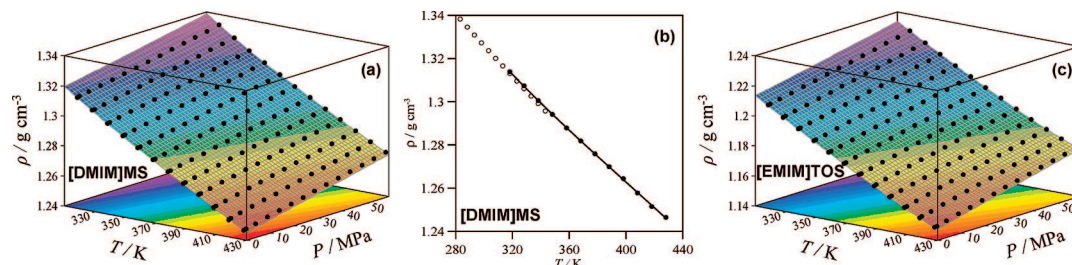


**Figure 5.** (●) Experimental density,  $\rho$ , as a function of pressure,  $P$ , and temperature,  $T$ , for [DMIM]MS and [EMIM]TOS. In panel b, the experimental data reported in this work at 0.1 MPa is compared with the literature values (○) from ref 57. Surfaces plotted in panels a and b correspond to TRIDEN fitting functions with parameters from Table S3 (Supporting Information). Contour plots are also plotted on bottom.

**TABLE 2: Parameters of Sanchez–Lacombe EOS<sup>55</sup> Obtained by Fitting to Experimental PVT Data<sup>a</sup>**

ionic liquid	$T^*/\text{K}$	$P^*/\text{MPa}$	$\rho^*/\text{kg m}^{-3}$	$r$	$\varepsilon^*/\text{J mol}^{-1}$	$v^*/\text{cm}^3 \text{ mol}^{-1}$	hard-core volume ( $v^* \times r$ )/ $\text{cm}^3 \text{ mol}^{-1}$	% AAD
[DMIM]MS	804.1	528.9	1364.9	12.1	6684.8	12.64	152.6	0.20
[EMIM]TOS	785.6	552.8	1260.0	19.0	6531.2	11.81	224.1	0.15

<sup>a</sup>  $T^*$ ,  $P^*$ ,  $\rho^*$  reduced characteristic parameters,  $r$  segment number of one molecule,  $\varepsilon^*$  segment interaction energy,  $v^*$  segment volume, and %AAD percentage absolute average deviation of the fitting.

overlapping with the acceptor LUMO and LUMO+1. The ion-pair frontier orbitals and those of the isolated cation and anion are rather similar. In fact, HOMO and HOMO−1 resemble those of the anion, and LUMO and LUMO+1 resemble those of the cation; hence, the covalent interaction in [DMIM]MS is minimal. Similar conclusions can be drawn for [EMIM]TOS. The resulting ion pairs are strongly polar structures, [DMIM]MS stronger compared to [EMIM]TOS, the polar character being more remarkable in position 2.

**Thermophysical Properties.** Sufficient literature data on ILs for theoretical and practical uses is lacking.<sup>24c</sup> Tables S1–S7 (Supporting Information) list the properties measured over wide pressure/temperature ranges. To our knowledge, Figure 5 shows the first PVT data available; the density data for [DMIM]MS at 0.1 MPa concur fairly well with those available at ambient pressure (Figure 5b),<sup>54</sup> but data for [EMIM]TOS were unavailable. The density values dropped along the isobars when the temperature was raised and rose with pressure along the isotherms. [EMIM]TOS has smaller densities because the size and shape of the TOS anion slightly hinders the packing (Figure 2). The [DMIM]MS densities are closer to those for  $\text{PF}_6^-$  imidazolium ILs,<sup>24c</sup> whose pseudo spherical anion favors an efficient packing.

To assemble further information, a simple PVT equation of state (EOS),<sup>55</sup> which is useful for ILs,<sup>24c</sup> was applied here. Such EOS nicely describes both ILs over wide pressure/temperature ranges; the least-squares fitting parameters and the (small) percentage deviations are listed in Table 2. The molar hard-core volume is a property defined as the total volume of one mole particles once excluded the free volume ( $V_F$ ), which can be evaluated as

$$V_F = V - v^*r \quad (5)$$

where  $V$  is the measured molar volume and  $v^*r$  is the EOS hard-core volume. Free volume is a valuable property closely related to solvation and gas solubility. The molar hard-core volume was remarkably larger for [EMIM]TOS. For [DMIM]MS it was even lower than for  $\text{PF}_6^-$  and  $\text{BF}_4^-$  imidazolium ILs,<sup>24c</sup> conveying an efficient packing (Table 2). As a rule, the weaker the anion/cation interaction, the larger the  $V_F$ .<sup>56</sup> The pressure and temperature effects on  $V_F$  are plotted in Figure 6.  $V_F$  was larger for [EMIM]TOS at any temperature and pressure, and

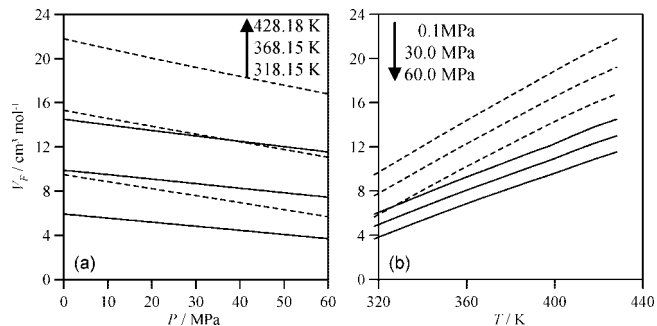


**Figure 6.** Free volume,  $V_F$ , of [DMIM]MS, continuous lines, and [EMIM]TOS, dashed lines, estimated from the Sanchez–Lacombe EOS with parameters from Table 2. (a) Panel shows isothermal results with the arrow indicating rising temperatures (from bottom to top) for both fluids, and (b) panel shows isobaric results with the arrow indicating rising pressures (from top to bottom) for both fluids.

for both fluids it rose remarkably with temperature and dropped gently with pressure. The markedly low  $V_F$  values (compared to the  $\text{PF}_6^-$  and  $\text{BF}_4^-$  imidazolium ILs)<sup>24c</sup> deduced for both fluids disclose the efficient packing, more striking for [DMIM]MS. The interaction energies were very close in position 1 (Figure 2), whereas in position 2 it was weaker for [EMIM]TOS. This finding could justify partially the larger [EMIM]TOS  $V_F$ , but it is the geometry effects of the planar TOS anion that mainly control the rise in the available  $V_F$ .

The derived properties isobaric thermal expansivity,  $\alpha_P$ , isothermal compressibility,  $k_T$ , and internal pressure,  $P_i$ , calculated from the PVT data using the TRIDEN fitting coefficients, are plotted in Figures 7–9. Normally  $\alpha_P$  is sensitive to the density/temperature function used,<sup>57</sup> an effect even more obvious for ILs whose compressibility is 2–3 times smaller compared to organic solvents; for instance, use of a linear function entails ignoring very subtle information on the fluid structure. To leave out any ambiguity, the high quality TRIDEN fitting function was used here. The  $\alpha_P$  values decreased for both ILs with rising pressure along the isotherms (regular behavior for most fluids) but, as the temperature was raised, they abnormally decreased along the isobars over the whole pressure/temperature range (Figure 7). Such a striking behavior in contrast to that of most fluids has been reported for imidazolium and pyridinium ILs.<sup>22b,23a,57,58</sup> In some instances, this effect was small; at 0.1 MPa,  $\alpha_P$  only dropped 2.6% for [1-butyl-3-methylimidazolium] $\text{PF}_6$  over a 45 K temperature range<sup>58</sup> and 2.7% for [1-octyl-

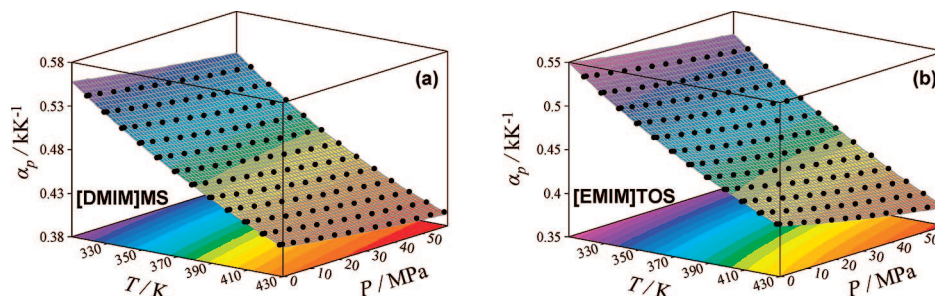


**Figure 7.** Calculated  $\alpha_p$  as a function of  $P$  and  $T$  for [DMIM]MS and [EMIM]TOS. Values calculated with TRIDEN functions using parameters from Table S3 (Supporting Information) at the working pressure and temperature (●) for the whole  $P/T$  range (surface). Contour plots are also plotted on bottom.

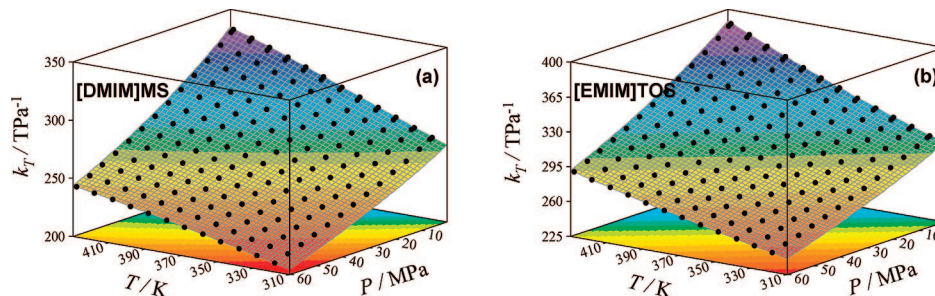


**Figure 8.** Calculated  $k_T$  as a function of  $P$  and  $T$ , for [DMIM]MS and [EMIM]TOS. Values calculated with the TRIDEN function using parameters from Table S3 (Supporting Information) at the working temperatures and pressures (●) over the whole  $P/T$  range (surface). Contour plots on bottom.

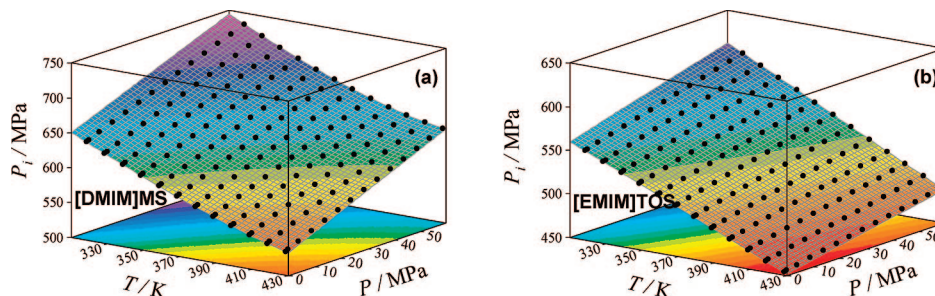


**Figure 9.** Calculated  $P_i$ , as a function of  $P$  and  $T$ , for [DMIM]MS and [EMIM]TOS. Values calculated with the TRIDEN function using parameters from Table S3 (Supporting Information) at the working temperature and pressure (●) over the whole  $P/T$  (surface). Contour plots on bottom.

3-methylimidazolium] $\text{BF}_4^-$  over a 50 K range.<sup>23a</sup> It could then be argued that this effect arises from use of misleading density/temperature fitting functions; however, that was not the case for [DMIM]MS and [EMIM]TOS because the observed fall in  $\alpha_p$  over a 110 K range was  $\sim 24\%$ , and was even larger at higher pressures (Tables S2–S3, Supporting Information). Therefore, a remarkable solid-like ordering may be concluded for the studied fluids, at least in the first solvation shell.

The  $k_T$  values plotted in Figure 8 (decrease with rising  $P$  along the isotherms and increase with rising  $T$  along isobars) adhere to the regular behavior, which is in agreement with the expected  $V_F$  variation with change in pressure/temperature. In line with the  $V_F$  values shown in Figure 6, [DMIM]MS is less compressible and more efficiently packed than [EMIM]TOS. The temperature effect on  $k_T$  diminishes the higher the pressure; at 0.1 MPa  $k_T$  rose for [EMIM]TOS by some 25.0% from 318.15 to 428.15 K, whereas at 60 MPa it increased by only 18.8%. Hence, a close-packed volume can be reached at high pressures.<sup>23a</sup>

The internal pressure,  $P_i$ , related to the cohesive forces, provides valuable information of fluids. A deal of confusion is observed in literature between this property and the cohesive energy density,  $c$ , defined as the sum of all attractive forces per unit volume that becomes broken whenever the liquid vaporizes,

and represents a measure of the full molecular cohesion.  $P_i$ , on the other hand, measures the work exerted against the cohesive forces by a liquid undergoing a small isothermal expansion, entailing changes in the internal energy; such an expansion is not necessarily accompanied by the disruption of all the intermolecular forces. Instead,  $P_i$  embraces mainly weak intermolecular forces strongly dependent on the separation distance, such as dispersion, repulsion, and being weakly dipolar. The two properties are equivalent only for nonassociated liquids; for associated ILs it turns out  $c > P_i$ .<sup>59</sup> The very large  $P_i$  values for high-temperature molten salts<sup>60</sup> with only pure electrostatic interactions show the relevance of this property for Coulomb fluids. The  $P_i$  values deduced for both ILs (Figure 9) are fairly large compared to other imidazolium ILs ([DMIM]MS  $\sim 200$  MPa and [EMIM]TOS  $\sim 100$  MPa larger).<sup>22b</sup> Hence, the ion packing entails very effective Coulomb interactions. The  $P_i$  values decreased with rising temperature along the isobars, because of the weakening of the intermolecular interactions, and rose with pressure along the isotherms, the latter feature showing that even at high pressures the attractive interactions prevail over repulsions for fluids with structures near close-packing.

The Hildebrand solubility parameter,  $\delta_H$ , defined as the square root of  $c$ , serves to characterize solubility phenomena. Evaluation

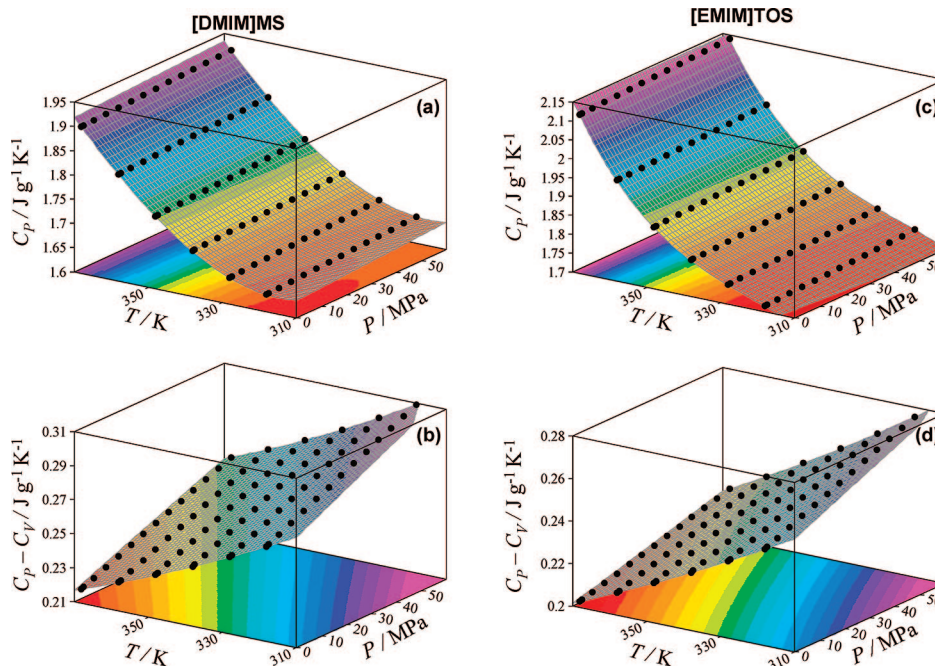


**Figure 10.** Experimental (0.1 MPa) and calculated (other pressures) isobaric heat capacity,  $C_p$ , and difference between isobaric and isochoric heat capacity,  $C_p - C_v$ , as a function of  $P$  and  $T$ , for [DMIM]MS and [EMIM]TOS. Values calculated with TRIDEN functions using parameters from Table S3 (Supporting Information) at the working  $T$  and  $P$  (●) and for the whole  $P/T$  range (surface). Contour plots on bottom.

of the  $\delta_H$  parameters requires, in turn, precise vaporization enthalpy data,  $\Delta H_{\text{vap}}$ ; however, due to the almost null volatility of ILs (a main green advantage versus organic solvents), measurement of reliable  $\Delta H_{\text{vap}}$  values is difficult.<sup>61</sup> Thus, if a reliable function linking the  $c$  and  $P_i$  parameters were available, then the  $P_i$  values deduced from experimental PVT data could afford the  $c$  and  $\delta_H$  parameters. We used earlier an empirical  $c/P_i$  function for imidazolium ILs,<sup>22b</sup> but the  $P_i$  values were remarkably lower than those for [DMIM]MS and [EMIM]TOS, and extrapolation to these ILs could be uncertain. Considering that such large cohesive energy density (the  $c$  values rise as  $P_i$  do) comes about by strong polar forces and specific H-bonding, stronger intermolecular forces in these ILs compared to imidazolium ILs can be surmised.

Isobaric heat capacity,  $C_p$ , is a useful tool to characterize ILs. The values collected (Figure 10) increased with temperature along the isobars. In line with the  $\alpha_p$  anomaly, they also increased with pressure along the isotherms, but the pressure effect was only little perceptible; for instance, a rise in pressure of 60 MPa s is accompanied by only 1.4%  $C_p$  enhancement for [EMIM]TOS at 318.15 K, and 0.9% at 428.15 K. Therefore, at higher temperatures an inversion to the “regular” trend is to be expected, that is, a decrease in  $C_p$  with rising pressure. Inasmuch as literature values are lacking, to stand a fair comparison we had to fall back on  $C_p$  data for related fluids. For instance, the [EMIM]TOS value at 348.15 K and 0.1 MPa ( $C_p = 1.863 \text{ J g}^{-1} \text{ K}^{-1}$ ) differs by only 5.9% with that of [1-butyl-3-methylimidazolium]TOS ( $C_p = 1.759 \text{ J g}^{-1} \text{ K}^{-1}$ ) evaluated at the same temperature under saturation conditions.<sup>63</sup> The data available for imidazolium-alkylsulfate ILs are few and controversial (Table 3); the data for [1-ethyl-3-methylimidazolium]-ethylsulfate ([EMIM]ES) by Fernández et al.<sup>64</sup> are remarkably larger than those by Zhang et al.,<sup>65</sup> whereas their values for [BMIM]MS are lower than those of Table 1. Our values for [DMIM]MS are close to those for [EMIM]ES, and both are lower than those of [1-butyl-3-methylimidazolium]octylsulfate ([BMIM]OS).<sup>22b</sup> Values for [EMIM]ES are very close to those for [BMIM]OS, which is striking in view that the larger number

**TABLE 3: Comparative Values of  $C_p/\text{J g}^{-1} \text{ K}^{-1}$  for Imidazolium-Alkyl Sulfate ILs at 318.15 K and 0.1 MPa**

[EMIM] ES <sup>68</sup>	[BMIM] MS <sup>68</sup>	[EMIM] ES <sup>69</sup>	[BMIM] OS <sup>24b</sup>	[DMIM]MS (this work)
1.97	1.19	1.62 <sup>a</sup>	1.900	1.636

<sup>a</sup> Measured under saturation conditions.

of vibrational degrees of freedom should raise the [BMIM]OS energy storage ability and, hence,  $C_p$ .<sup>62</sup> The results by Fernández et al.<sup>64</sup> show that a 65.5% boost in  $C_p$  appears from [BMIM]MS to [EMIM]ES, a feature justifiable considering the different degrees of freedom of both fluids.

Use of ILs, as heat transfer/thermal storage fluids for industrial applications, requires  $C_p$  data over wide pressure/temperature ranges.<sup>66</sup> A suitable thermal storage IL should meet the following features: (i) low volatility, (ii) wide liquid range, (iii) high thermal storage density, and (iv) low viscosity. ILs meet condition (i), thus leaving out the hazards inherent to most commercial fluids. The [DMIM]MS decomposition temperature (396 °C)<sup>17</sup> assures a ~350 °C liquid range; for [EMIM]TOS such a figure was unavailable but, considering related compounds,<sup>63</sup> a ~250 °C range can be surmised. Thermal storage densities for 100 °C differential are 215 and 207 MJ m<sup>-3</sup> for [DMIM]MS and [EMIM]TOS, respectively, commensurate with those used in industry. Viscosities (next paragraph), slightly larger than those of synthetic fluids, dropped remarkably from low to high temperatures, thus allowing an efficient use in pumping systems that only would be questionable at low temperatures. Hence, both ILs are suitable as thermal storage systems, [DMIM]MS more favorably.

Viscosities for both ILs over wide pressure/temperature ranges together with the fitting of eqs 1 and 2 and the derived properties calculated with eqs 3 and 4 are listed in Tables S4–S7 (Supporting Information). The pressure and temperature effects are shown in Figure 11. Despite the recognized significance of reliable and accurate viscosities, only ambient pressure data were found for both ILs (for [EMIM]TOS only a single point, inserted

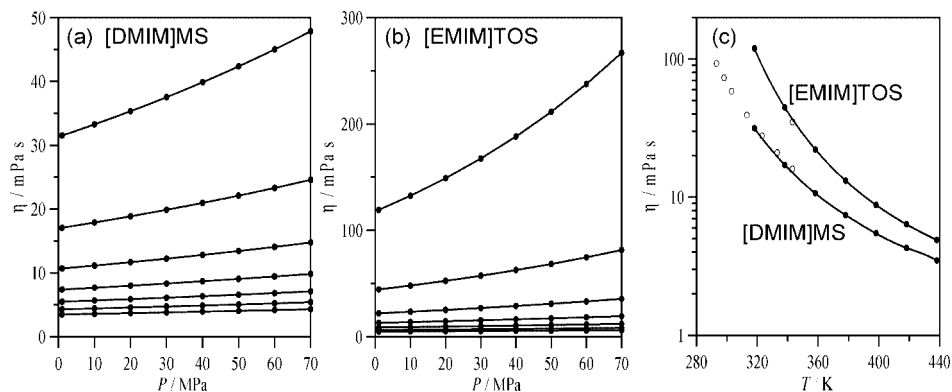


**Figure 11.** (●) Dynamic viscosity,  $\eta$ , as a function of  $P$  and  $T$  for [DMIM]MS and [EMIM]TOS. (a,b) From top to bottom: 318.15, 338.15, 358.15, 378.15, 398.15, 418.15, and 438.15 K. Lines: fitting function, eqs 1 and 2, with parameters from Table S5 (Supporting Information). In (c) measured data at 0.1 MPa (●) compared with values from refs 29 and 57 (○).

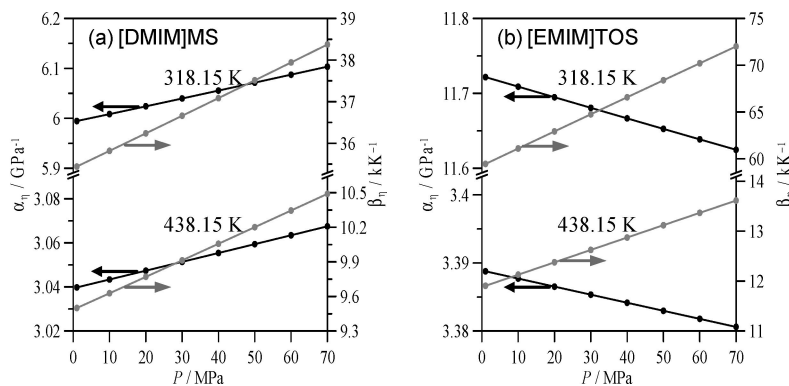


**Figure 12.**  $\alpha_\eta$  and  $\beta_\eta$  as a function of  $P$  and  $T$  for [DMIM]MS and [EMIM]TOS. Coefficients calculated from parameters reported in Table S5 (Supporting Information).

In Figure 11c), the good agreement validating our experimental methodology.<sup>22b</sup> The viscosities of both ILs are the same order of magnitude as those of other imidazolium ILs, but [EMIM]-TOS is clearly more viscous than [DMIM]MS; for [EMIM]-TOS, viscosities were twice or even three times as much as those for [BMIM][BF<sub>4</sub>] and for [DMIM]MS they were half-the [BMIM][PF<sub>6</sub>] values.<sup>24a</sup> Viscosities became close to those of organic solvents upon increasing temperature; hence, application in heat/mass transfer would be more efficient at temperatures far from the melting point, where viscosities are too high. Viscosities increased linearly with pressure, sharply at low temperatures and softly at high temperatures. Pressure and temperature affected viscosities unevenly. At 1 MPa, a boost from 318.15 to 428.15 K brought about 88.9% fall for [DMIM]MS and 95.9% for [EMIM]TOS, whereas at 328.15 K, a boost from 1 to 70 MPa yielded 52.1% rise for [DMIM]MS and 123.7% for [EMIM]TOS. The larger pressure effect on [EMIM]TOS accounts for a less compact packing. [EMIM]TOS is more viscous because the ion shape hinders both the packing and the flow, the more so the higher the pressure, thus pushing molecules one against another, with larger interactions and a gradually hindered flow.

The pressure ( $\alpha_\eta$ ) and temperature ( $\beta_\eta$ ) viscosity coefficients (eqs 3 and 4) are plotted in Figure 12. The  $\alpha_\eta$  values are lower for [DMIM]MS at all temperatures and pressures, and for both ILs they decreased with a rise in temperature; this feature concurs with the larger  $V_F$  available at higher temperatures, which diminishes the pressure effect. The larger values for [EMIM]TOS rely on the larger  $(\partial\eta/\partial P)$  values (Figure 11), which counteract the lower  $(1/\eta)$  values (eq 3) due to the size and shape of the TOS anion. The less compact packing for [EMIM]TOS favors a marked pressure effect, and the  $\alpha_\eta$  values

at 318.15 K double (roughly) those for [DMIM]MS. This effect diminishes at low temperatures. As the temperature was raised, the  $\alpha_\eta$  difference for both ILs decreased because  $V_F$  is large and the pressure effects become balanced. The pressure effect on  $\alpha_\eta$  is small, and differs for both liquids; at constant temperature, it rises for [DMIM]MS with a boost in pressure, whereas for [EMIM]TOS it shows the opposite trend (Figure 12).  $\beta_\eta$  decreased with rising temperature and rose with a boost in pressure and was lower for [DMIM]MS.

ILs conductivity attracts a high rate of interest for sensors and batteries and provides valuable information on ionic association.<sup>67</sup> Conductivity relies on the number and mobility of the charge carriers involved and is related to viscosity and self-diffusion coefficients through the Stokes–Einstein equation.<sup>68</sup> Figure 13 displays the ionic conductivities for the studied ILs as a function of temperature. Ionic conductivity was larger for [DMIM]MS at all temperatures, an effect heightened at lower temperatures (8 times larger at 278.15 K and only 2 times at 368.15 K). Hence, the cation/anion interaction is stressed for [EMIM]TOS; the size and shape of the TOS anion slows down its diffusion compared to MS, thus leading to lower ion mobility and conductivity and higher viscosity. As the temperature is raised, the ion mobility is enhanced by the weakening of the ion pairs, the diffusion increase brings about larger conductivities, and the behavior of both ILs become closer. The temperature effect on the ion conductivity is nicely described by the Vogel–Fulcher–Tammann (VFT) equation<sup>69</sup>

$$\sigma = \sigma_0 \exp(-B/(T - T_0)) \quad (6)$$

where  $T_0$  is the Vogel temperature, normally 10–30 K lower than the glass transition temperature. The least-squares fitting

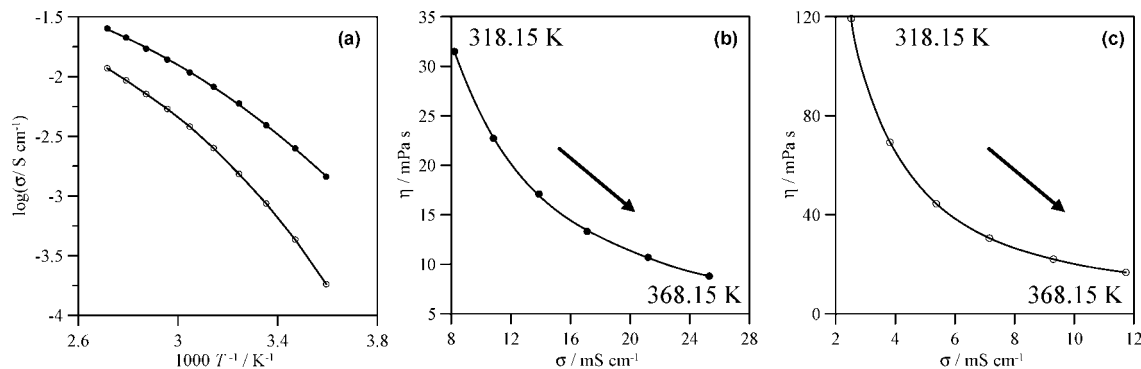


**Figure 13.** (a) Experimental conductivity,  $\sigma$ , at atmospheric pressure as a function of  $T$ ; (b,c) Relationship between viscosity,  $\eta$  (at 1 MPa), and conductivity (at atmospheric pressure). Arrows point rising temperature. (●) [DMIM]MS and (○) [EMIM]TOS. Lines plotted in panel a show VFT fits (parameters:  $\sigma_0 = 680, 414 \text{ mS cm}^{-1}$ ;  $B = 642, 593 \text{ K}$ ;  $T_0 = 173, 202 \text{ K}$ ; for [DMIM]MS and [EMIM]TOS, respectively) and lines in panels b and c show trends.

parameters are reported in Figure 13. The fragility parameter,  $F$ , defined in eq 7, reflects the change of the glassy structure as the temperature rises above the glass transition temperature

$$F = \frac{B}{T_0} \quad (7)$$

According to Angell's<sup>70</sup> nomenclature, the values  $F = 3.7$  for [DMIM]MS and 2.9 for [EMIM]TOS prove that [EMIM]-TOS is more fragile, that is, more viscous and less conductive. Although a rise in temperature disrupts the [EMIM]TOS glassy structure more rapidly and is accompanied by a heightened conductivity and fluidity, its tendency to develop interactions is somewhat stronger compared to [DMIM]MS, and thus [EMIM]TOS is more viscous and less conductive. Hence, the cohesive forces/fragility factors interplay is critical to determine the ILs structure.<sup>71</sup> Moreover, the results shown in Figures 13b,c give away a pronounced nonlinear viscosity/conductivity correlation for both ILs, occasioned by the highly nonlinear viscosity-temperature behavior. Likewise, these plots account for the lower conductivities deduced at larger viscosities and lower ionic mobilities; the notable fall in viscosity with rising temperature entails an appreciable gain in conductivity.

The viscosity behavior of ILs bears close connection with large scale rearrangements, and the linkage with ionic conductivity shows that it also bears relation with microscopic dynamics.<sup>69,72</sup> Ionic conductivity for these ILs is viscosity-diffusion controlled.<sup>68</sup> The relation between viscosity and conductivity may be analyzed properly by use of the Walden plots,<sup>71</sup> in which the specific conductivity log function is plotted vs log of fluidity. This method allows one to infer crucial structural information on the ILs structure.<sup>71,73</sup> Figure 14 shows a Walden plot for the two ILs studied; although both lie below the ideal line, the deviations were somewhat modest (0.44 and 0.30 at 368.15 K for [DMIM]MS and [EMIM]TOS, respectively). In other words, although certain extent of ion pairing is to be expected in the fluid and therefore a slight volatility, this is less than for other ILs. This behavior bears out a diffusion controlled conductivity regime instead of the presence of relevant ion pairs.

**Molecular Dynamics.** Classical MD simulations add interesting structural features. The OPLS-AA force field parameters used in the simulations are listed in Tables S8–S12 (Supporting Information). ILs exhibit low diffusion rates, and therefore MD simulations must be extended long enough to capture the main features. The simulations reported were carried out for 5 ns;

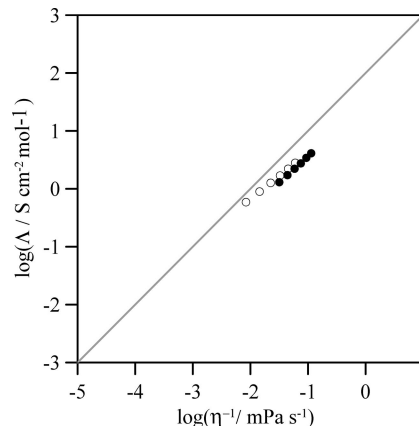


**Figure 14.** Walden plot for (●) [DMIM]MS and (○) [EMIM]TOS over the 318.15–368.15 K temperature range.  $\Lambda$  = molar conductivity and  $\eta$  = dynamic viscosity.

Figure II (Supporting Information) shows that the results remain roughly the same upon enlarging 4 times the simulation time, and thus 5 ns suffices to infer the main structural features. To validate the force field parametrization and to ensure the structural features deduced, the calculated properties are compared with experiments. Densities and isobaric thermal expansivities are plotted in Figure 15. The simulated densities were always lower than those measured, with 1.9–2.1% deviation (roughly) for [DMIM]MS and 2.3–3.0% for [EMIM]TOS (Table S13, Supporting Information). Considering the predictive nature of the calculations, the good agreement reached is in line with recent studies<sup>74</sup> and parametrizations of imidazolium/alkylsulfate ILs.<sup>75</sup> The larger deviations for [EMIM]TOS can be due to the packing effects of the TOS ring, not fully accounted for by the force field; hence, refined Lennard-Jones parameters for the TOS anion would increase the densities, a task to be undertaken in near the future. Nevertheless, the agreement reached is reasonable and lends solid insights into the liquid property and structure.

Prediction of isobaric thermal expansivities may drop a hint on the simulation ability to capture the density changes with temperature; the difficulties inherent to predicting  $\alpha_p$  values should be appraised. Using well-known fluctuation equations in the NPT ensemble,<sup>74a</sup> the  $\alpha_p$  values were predicted from simulations with deviations in the (−10, +10)% range for [DMIM]MS and (−5, +15)% for [EMIM]TOS (Figure 15c). Although such deviations may seem large, they are in fact consistent with literature predictions.<sup>74</sup> The overall  $\alpha_p$  trend was nicely captured by the simulation, even the abnormal trend,

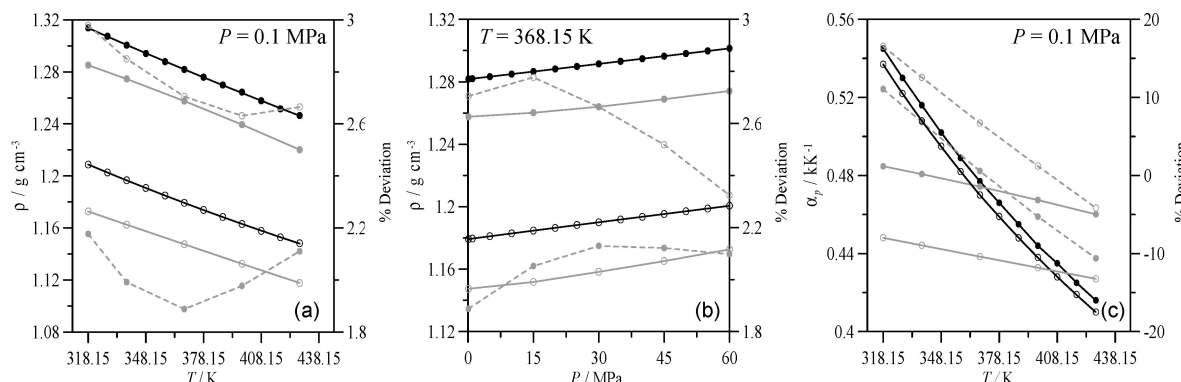


**Figure 15.** Experimental and computed (OPLS-AA molecular dynamics simulations) thermophysical properties as a function of  $P$  and  $T$  for [DMIM]MS and [EMIM]TOS. Density,  $\rho$ , and isobaric thermal expansivity,  $\alpha_p$ . Filled circles, [DMIM]MS; empty circles, [EMIM]TOS; black symbols and lines, experimental; gray symbols and lines, computed; dashed lines with symbols, %AAD.

assuring that such a behavior is by no means a mathematical artifact, but rather an outcome of the highly structured studied fluids.

Other promising properties bearing valuable information are also listed in Table S13 (Supporting Information), but lack of literature data made it unfeasible to stand comparison. The Coulomb and van der Waals liquid phase intermolecular energy diminished with rising temperature, slightly increased with rising pressure, and were always lower for [DMIM]MS, which is in agreement with the smaller viscosities and greater molar conductivities. The van der Waals contributions dropped with a rise in temperature (18% decrease for [DMIM]MS and 17% for [EMIM]TOS within 110 K), whereas the Coulomb terms (~90% for [DMIM]MS and ~95% for [EMIM]TOS) reinforce that the liquids are dominated by Coulomb interactions, concurrent with other imidazolium ILs.<sup>76</sup> The lower internal pressures for [EMIM]TOS (Tables S1, S2, Supporting Information) show that short-range interactions are less effective than for [DMIM]MS. The stronger forces (Coulomb and H bonding) are more effective in [EMIM]TOS.

Vaporization enthalpy,  $\Delta H_{\text{vap}}$ , an important property closely related to intermolecular forces, was calculated from MD simulations as

$$\Delta H_{\text{vap}} = \Delta U_{\text{L,G}} + RT = (U_{\text{G,inter}} - U_{\text{L,inter}}) + (U_{\text{G,intra}} - U_{\text{L,intra}}) + RT \quad (8)$$

where  $U$  stands for the molar internal energy of the liquid (L) and gas (G) phase, intra refers to intramolecular (bond, angle, dihedral, and nonbonded intramolecular interactions) and inter refers to intermolecular (Coulomb and van der Waals) contributions to internal energy. To calculate gas-phase properties, the single ion-pair simulated was regarded as a gas-phase model, which is in agreement with experimental and simulation studies.<sup>74a,77,78</sup> The simulation allows to split the vaporization enthalpy into different contributions. The intramolecular energy difference between liquid and gas is  $\sim 5$  kJ mol<sup>-1</sup> for both ILs with only a small change with temperature; the larger liquid density (the tighter ion packing conveys a weak effect on the geometry parameters) justifies such a small difference. The kinetic energy difference between vapor and liquid lies around 0.6 kJ mol<sup>-1</sup> for both ILs. Intramolecular and kinetic contributions to the vaporization enthalpy is almost negligible, and hence the Coulomb and van der Waals contributions dominate.<sup>78</sup> The vaporization enthalpies (Table S13, Supporting Information), which are larger for [EMIM]TOS, are below 200 kJ mol<sup>-1</sup>,

which is the common range for ILs.<sup>61</sup> Coulomb and van der Waals contributions are  $\sim 75/25\%$  for [DMIM]MS and  $\sim 85/15\%$  for [EMIM]TOS. It should be pointed out that the gas-phase was modeled considering ion-pairs, thus the Coulomb contribution is appreciable. Though van der Waals contributions were considerable, they were lower than for other imidazolium ILs,<sup>78</sup> especially true is for [EMIM]TOS, whose aromatic rings hinder the van der Waals growth compared to [DMIM]MS, whose smaller anion favors a closer contact and larger contributions.

Of importance to characterize solvents are the cohesive energy density,  $c$ , and the Hildebrand solubility parameter,  $\delta$ . The calculated  $c$  values (Table S13, Supporting Information), as expected for low volatile fluids dominated by Coulomb forces, are large compared to organic solvents. Despite the lower vaporization enthalpy for [DMIM]MS, the  $c$  values are larger due to the higher densities, which lead to a greater energy density per volume unit. The  $c$  values for both fluids are in the range of other imidazolium ILs,<sup>74a,79,80</sup> and the  $\delta$  parameters are close to those of polar solvents such as methanol  $\delta = 29.3$  MPa.<sup>81</sup>

Radial distribution functions (RDFs) may provide valuable information on liquid features. The maxima and minima shown in Figures 16 and 17 reveal that the long-range ordering remains even beyond the 15 Å limit distance. The cation/anion RDFs through positions 1 and 2 bring interesting conclusions. For position 1, the RDFs (D4-M6, and E4-T10) show peaks sharper and narrower than for position 2 (D2-M6 and E1-T10). It should be noted that the shape and interaction through positions 1 and 2 are similar for both ILs and for ([BMIM]OS)<sup>22b</sup> and [BMIM]PF<sub>6</sub>,<sup>82</sup> hence, the preference for 1 is only weakly affected by the anion. Interaction through position 1 shows three well-defined peaks at 3.9, 5.9, and 11 Å for both ILs, whereas position 2 provides a wider first peak at 4.1 Å in agreement with DFT calculations (Figure 2), and a second at 10.8 Å. This behavior shows subtle effects on the solvation shell around the cation. Three short-range solvation levels can be recognized; the first two shells around position 1 are well defined, whereas around position 2 they seem to merge into a wider peak for both fluids. The interactional effect with both H atoms in position 2 probably hinders a well-defined second shell. It is noteworthy that, despite the larger TOS size, the maxima appear at nearly the same distance and the TOS peaks were only slightly weaker. Thus, although the anion/cation interaction through position 1 seems more efficient, in position 2 the anions lie at a slightly larger distance of the interacting cation, yielding a wider first solvation shell instead of two narrow ones. The third

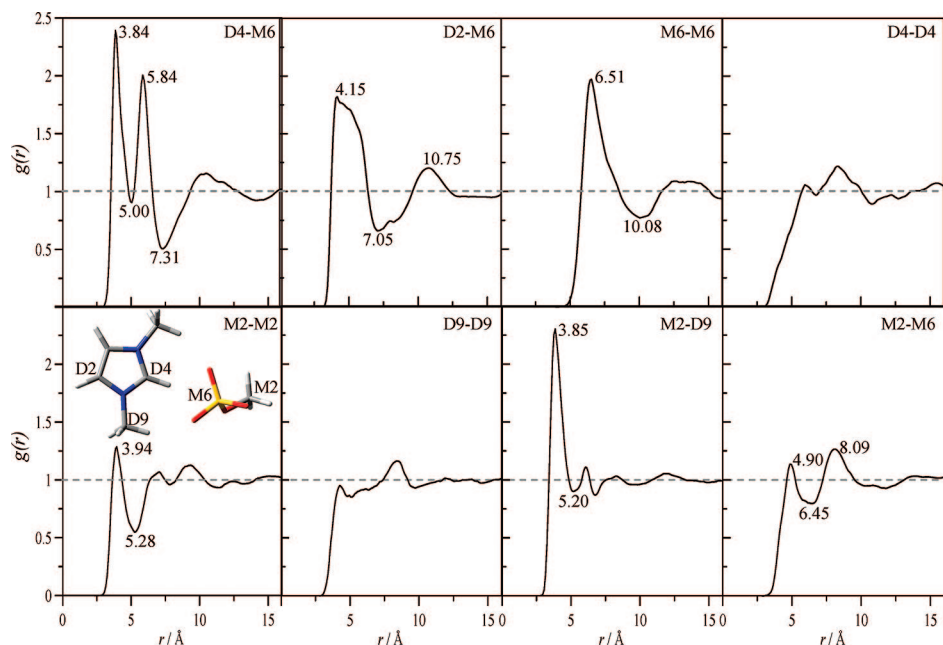


**Figure 16.** Site–site radial distribution functions,  $g(r)$ , for [DMIM]MS calculated from OPLS-AA molecular dynamics simulations at 318 K and 0.1 MPa. Atom numbering as an inset.

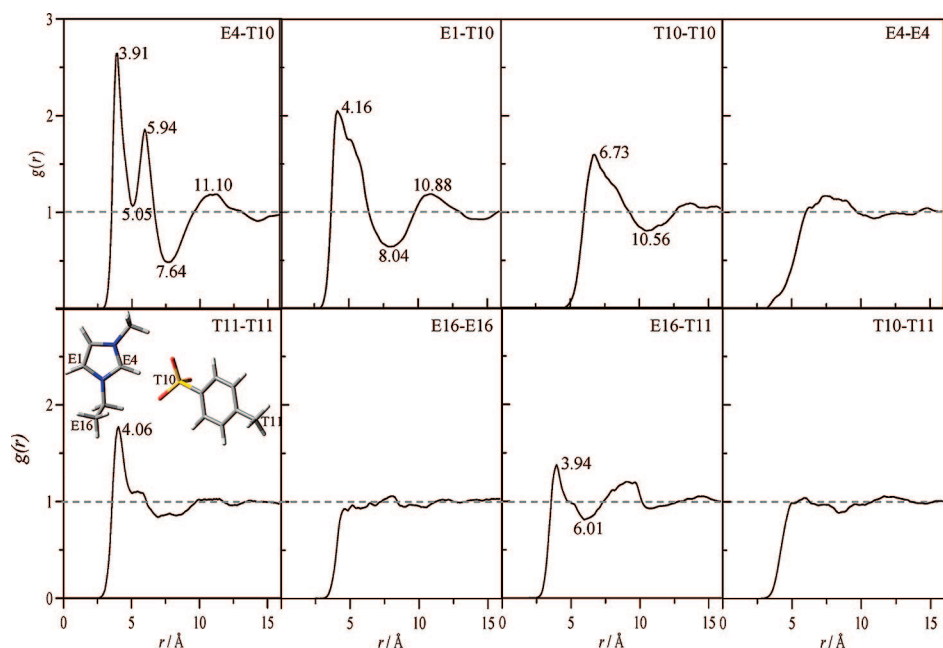


**Figure 17.** Site–site radial distribution functions,  $g(r)$ , for [EMIM]TOS calculated from OPLS-AA molecular dynamics simulations at 318 K and 0.1 MPa. Atom numbering as an inset.

maximum for position 1 and the second for position 2 appeared at nearly the same distance, showing that the difference between position 1 and 2 for cations determine the short-range interaction structure.

RDFs analyses of M6-M6 (sulfur–sulfur), M2-M2 (carbon–carbon) and M2-M6 atoms in [DMIM]MS unveil anion/anion structuring. M6-M6 gives a broad peak at 6.51 Å due to the secondary order introduced by the cation/anion interaction. M2-M2 shows a sharp maximum at a short distance, pointing to a certain anion aggregation of methyl groups in the solvation sphere around the cation. The sharp and intense M2-D9 RDF, showing the interaction between the cation and anion methyl groups, also points to aggregation of methyl groups in the solvation sphere around the cation. The (D4-D4 and D9-D9) cation–cation interaction shows no noticeable features, denoting

that the [DMIM]MS structure is controlled by the anion solvation around the imidazolium cation. The results for TOS are similar; only the slight difference brought about by the bulky TOS anion in the cation solvation sphere apparently hinders the aggregation growth of the terminal methyl groups (weaker RDF for E16-T11 in TOS than for M2-D9 in MS). The solvation around the imidazolium cation is characterized by successive solvation shells, where the apolar anion chains tend to aggregate among them and with those of the cation (at least in the first solvation sphere).

The anion spatial arrangement around the cation in the solvation shell affords additional features. The probability distribution function displayed for certain angles and dihedrals (Figures 18 and 19) points up the anion placed around the cation. The probability function for the  $\theta$  angle shows that the anion

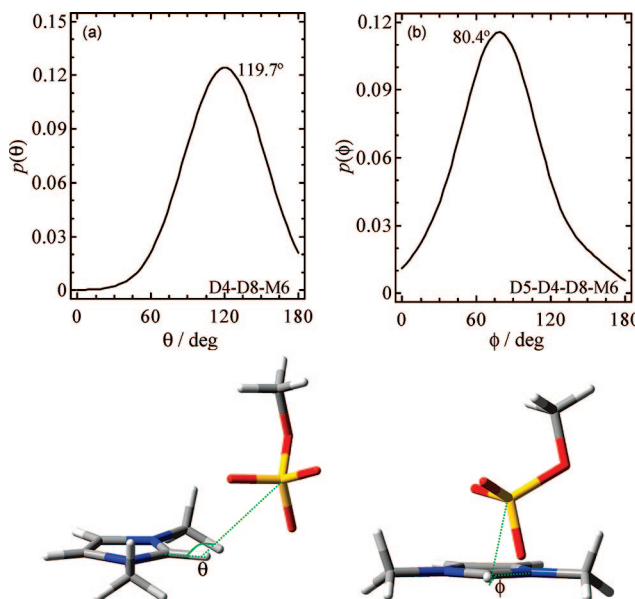


**Figure 18.** Probability distribution functions for the angles and dihedrals in [DMIM]MS calculated from OPLS-AA molecular dynamics simulations at 318 K/0.1 MPa. Atom numbering as in Figure I (Supporting Information).

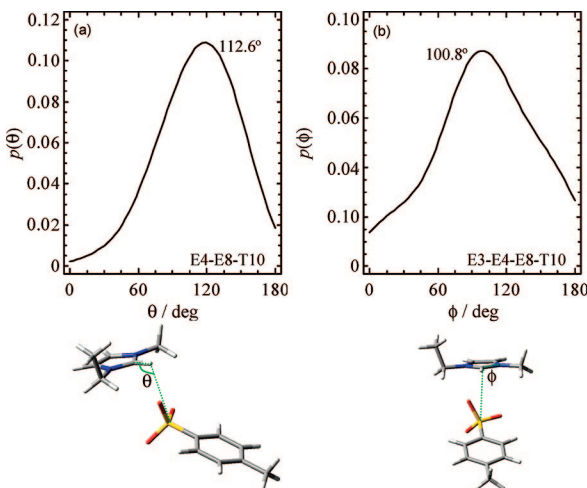


**Figure 19.** Probability distribution functions for angles and dihedrals in [EMIM]TOS calculated from OPLS-AA molecular dynamics simulations at 318 K/0.1 MPa. Atom numbering as in Figure I (Supporting Information).

lies over the imidazolium plane with a  $119.7^\circ$  angle for MS and slightly lower for TOS. The  $\phi$  dihedral angle shows that the anion/cation interaction in position 1 goes on with the anion acting from the top of the imidazolium ring with the negative charge placed in the center ring site. This behavior is in contrast with the preferred in-plane interaction deduced from DFT gas calculations; the presence of neighbor molecules in the liquid-phase leads to out-of-plane interactions that favor an easier ion packing.

The dynamic behavior of both ILs was studied using the self-diffusion coefficient,  $D$ , calculated with the Stokes–Einstein equation

$$D = \frac{1}{6} \lim_{t \rightarrow \infty} \frac{d}{dt} \langle \Delta r(t)^2 \rangle \quad (9)$$

where the quantity in brackets is the mean square displacement, msd. The cation and anion msd values, calculated with MD

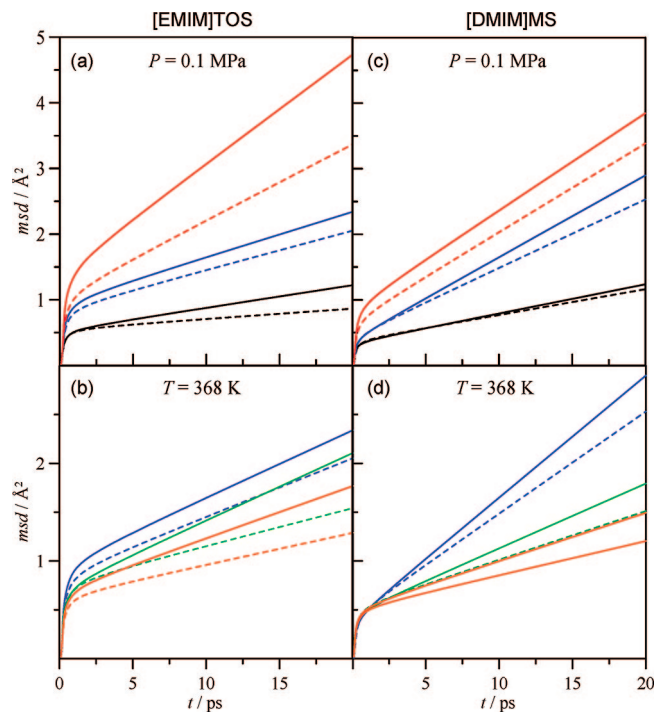


**Figure 20.** Temperature and pressure effect on the mean square displacement, msd, for [DMIM]MS and [EMIM]TOS calculated from OPLS-AA molecular dynamics simulations. In panels (a) and (c): (black) 318 K/0.1 MPa, (blue) 368 K/0.1 MPa, (red) 428 K/0.1 MPa. In panels (b) and (d): (blue) 368 K/0.1 MPa, (green) 368 K/30 MPa, (red) 368 K/60 MPa. Continuous lines, msd for cation; dashed lines, msd for anion.

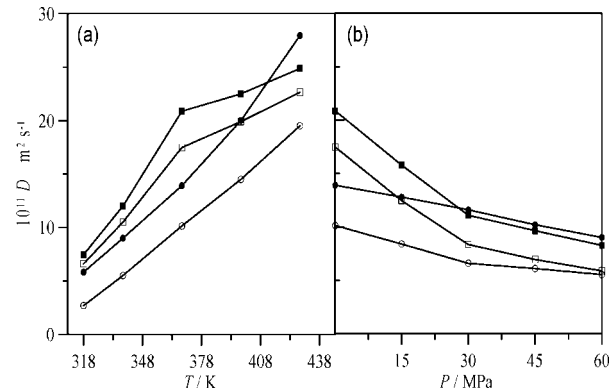


**Figure 21.** Temperature and pressure effect on the self-diffusion coefficient,  $D$ , for [DMIM]MS and [EMIM]TOS calculated from OPLS-AA molecular dynamics simulations. (■) [DMIM]<sup>+</sup>, (□) MS<sup>-</sup>, (●) [EMIM]<sup>+</sup>, and (○) TOS<sup>-</sup>. Continuous lines plotted to show trends.

(Figure 20), are reported for the first 20 ps simulation (after equilibration) as a function of pressure and temperature. The slope of the linear fitting provides the  $D$  coefficients (Table S13, Supporting Information, Figure 21). The  $D$  values for cations were larger than for anions over the whole  $P/T$  ranges, as are for other ILs.<sup>24b,79</sup> Moreover, the overall  $D$  values, calculated as  $0.5(D_{\text{cation}} + D_{\text{anion}})$ , are larger for [DMIM]MS, concurrent with the lower viscosity and larger conductivity compared to [EMIM]TOS.

### Concluding Remarks

The combination of experimental and computational studies of the selected ILs has come to valuable conclusions. The properties measured over wide  $P/T$  ranges provide useful data

for process design, revealing these ILs as suitable candidates in different applications. High density, moderate viscosity (similar to that of organic solvents), and high thermal storage ability are the main features. The abnormal  $\alpha_p$  and  $C_p$  values point to highly structured fluids. Viscosity and conductivity analyses reveal diffusion controlled process and fluids categorized as fragile. The DFT gas-phase results show that interactions through positions 1 and 2 of the imidazolium ring are likely with a slight stabilization through position 1. Charge transfer analyses discard covalent interactions for both fluids. The molecular dynamics calculations lead to satisfactory predictions of thermophysical properties over the  $P/T$  ranges studied, thus validating the force field parametrization of the simulations. Reasonable vaporization enthalpy, cohesive energy density, and Hildebrand parameters were deduced. The analysis of the energy contributions reveals mainly Coulomb contributions with weaker van der Waals terms. The structural features deduced from MD simulations show a strongly ordered fluid with well-defined long distance solvation shells.

**Acknowledgment.** The financial support by Junta de Castilla y León, Project BU-020A/07, and Ministerio de Educación y Ciencia, Project CTQ2005-06611/PPQ, Cofinanced Feder, (Spain), is gratefully acknowledged.

**Supporting Information Available:** Table S1 (experimental and calculated properties for [DMIM]MS as a function of pressure and temperature), Table S2 (experimental and calculated properties for [EMIM]TOS as a function of pressure and temperature), Table S3 (TRIDEN fitting parameters for [DMIM]MS and [EMIM]TOS), Table S4 (experimental dynamic viscosity for [DMIM]MS and [EMIM]TOS as a function of pressure and temperature), Table S5 (fitting parameters of dynamic viscosity for [DMIM]MS and [EMIM]TOS), Table S6 (temperature and pressure coefficients for [DMIM]MS and [EMIM]TOS), Table S7 (experimental ionic conductivity for [DMIM]MS and [EMIM]TOS), Figure I (atom numbering for [DMIM]MS and [EMIM]TOS), Table S8 (calculated MK atomic charges for [DMIM]MS and [EMIM]TOS), Tables S9–S12 (OPLS-AA force field parameters for [DMIM]MS and [EMIM]TOS), Figure II (comparison of 5 and 20 ns MD simulations), Table S13 (properties of [DMIM]MS and [EMIM]TOS computed from molecular dynamics simulations). This material is available free of charge via the Internet at <http://pubs.acs.org>.

## References and Notes

- (a) Anastas, P.; Warner, J. *Green Chemistry. Theory and Practice*; OUP: Cambridge, 1998; (b) Lancaster, M. *Green Chemistry. An Introductory Text*; RSC: Cambridge, 2002.
- (a) Graedel, T. *Green Chem.* **1999**, *1*, G126. (b) Anastas, P.; Lankey, R. L. *Green Chem.* **2000**, *2*, 289. (c) Martel, A. E.; Davies, J. A.; Olson, W. W.; Abraham, M. A. *Annu. Rev. Environ. Resour.* **2003**, *28*, 401.
- Ionic Liquids as Green Solvents. Progress and prospects*; Rogers, R. D.; Seddon, K. R., Eds.; ACS: Washington, DC, 2003.
- Sheldon, R. A. *Green Chem.* **2005**, *7*, 267.
- Álvaro, M.; Carbonell, E.; Ferrer, B.; García, H.; Herance, J. R. *Photochem. Photobiol.* **2006**, *82*, 185.
- Electrochemical Aspects of Ionic Liquids*; Ohno, H., Ed.; Wiley-Interscience: New York, 2005.
- Gottfried, J. M.; Maier, F.; Rossa, J.; Gerhard, D.; Schulz, P. S.; Wasserscheid, P.; Steinrück, H. P. *Z. Phys. Chem.* **2006**, *220*, 1439.
- Rogers, R. D. *Nature (London)* **2007**, *447*, 917.
- Plechkova, N. V.; Seddon, K. R. Designer Solvents for Green Chemistry. In *Methods and Reagents for Green Chemistry*; John Wiley & Sons: New York, 2007; pp 105–130.
- Holbrey, J. D.; Seddon, K. R. *Clean Prod. Processes* **1999**, *1*, 223.
- Hough, W. L.; Rogers, R. D. *Bull. Chem. Soc. Jpn.* **2007**, *80*, 2262.
- (a) Kobrak, M. N. *Green Chem.* **2008**, *10*, 80. (b) Jork, C.; Kristen, C.; Pieraccini, D.; Stark, A.; Chiappe, C.; Beste, Y. A.; Arlt, W. *J. Chem. Thermodyn.* **2005**, *37*, 537.
- (a) Brennecke, J.; Letcher, T.; Goodwin, A. R. H. *J. Chem. Thermodyn.* **2005**, *37*, 523. (b) Brennecke, J.; Maginn, E. J. *AIChE J.* **2001**, *47*, 2384.
- Zhao, D.; Liao, Y.; Zhang, Z. *Clean* **2007**, *35*, 42.
- Jastorff, B.; Möller, K.; Behrend, P.; Bottin-Weber, U.; Filser, J.; Heimersm, A.; Ondruschka, B.; Ranke, J.; Schaefer, M.; Schröder, H.; Stark, A.; Stepnowski, P.; Stock, R.; Störmann, R.; Stolte, S.; Wels, U.; Ziegert, S.; Thöming, J. *Green Chem.* **2005**, *7*, 362.
- Cho, C. W.; Pham, T. P. T.; Jeon, Y. C.; Yun, Y. S. *Green Chem.* **2008**, *10*, 67.
- Holbrey, J. D.; Reichert, W. M.; Swatloski, R. P.; Broker, G. A.; Pitner, W. R.; Seddon, K. R.; Rogers, R. D. *Green Chem.* **2002**, *4*, 407.
- (a) Matsumoto, M.; Mochiduki, K.; Fukunishi, K.; Kondo, K. *Sep. Purif. Technol.* **2004**, *40*, 97. (b) Stepnowski, P.; Stładanowski, A. C.; Ludwiczak, A.; Laczyńska, E. *Eur. Hum. Exp. Toxicol.* **2004**, *23*, 513.
- Burrell, A. K.; Del Sesto, R. E.; Baker, S. N.; McCleskey, T. M.; Baker, G. A. *Green Chem.* **2007**, *9*, 449.
- Stolte, S.; Arning, J.; Bottin-Weber, U.; Matzke, M.; Stock, F.; Thiele, K.; Uerdinger, M.; Welz, U.; Jastorff, B.; Ranke, J. *Green Chem.* **2006**, *8*, 621.
- Gathergood, N.; Scammells, P. J.; García, M. T. *Green Chem.* **2006**, *8*, 156.
- (a) Wasserscheid, P.; van Haal, R.; Bösmann, A. *Green Chem.* **2002**, *4*, 400. (b) Dávila, M. J.; Aparicio, S.; Alcalde, R.; García, B.; Leal, J. M. *Green Chem.* **2007**, *9*, 221.
- (a) Gu, Z.; Brennecke, J. F. *J. Chem. Eng. Data* **2002**, *47*, 339. (b) Esperança, J. M.; Visak, Z. P.; Plechkova, N. V.; Seddon, K. R.; Guedes, H. J.; Rebelo, L. P. *J. Chem. Eng. Data* **2006**, *51*, 2009. (c) Kandil, M. E.; Marsch, K. N. *J. Chem. Eng. Data* **2007**, *52*, 2382. (d) Machida, H.; Sato, Y.; Smith, R. L. *Fluid Phase Equilib.* **2008**, *264*, 147.
- (a) Tomida, D.; Kumagai, A.; Qiao, K.; Yokohama, C. *Int. J. Thermophys.* **2006**, *27*, 39. (b) Harris, K. R.; Kanakubo, M.; Woolf, L. A. *J. Chem. Eng. Data* **2006**, *51*, 1161. (c) Harris, K. R.; Kanakubo, M.; Woolf, L. A. *J. Chem. Eng. Data* **2007**, *52*, 2425.
- Lee, S. U.; Jung, J.; Han, Y. K. *Chem. Phys. Lett.* **2005**, *406*, 332.
- Domanska, U.; Zolek-Tryznowska, Z.; Krolikowski, M. *J. Chem. Eng. Data* **2007**, *52*, 1872.
- Strehmel, V. *Macromol. Symp.* **2007**, *254*, 25.
- Seddon, K. R.; Stark, A.; Torres, M. J. *Pure Appl. Chem.* **2000**, *72*, 2275.
- (a) García, B.; Aparicio, S.; Alcalde, R.; Dávila, M. J.; Leal, J. M. *Ind. Eng. Chem. Res.* **2004**, *43*, 3205. (b) Aparicio, S.; García, B.; Alcalde, R.; Dávila, M. J.; Leal, J. M. *J. Phys. Chem. B* **2006**, *110*, 6933.
- Lemon, E. W.; McLinden, M. O.; Friend, D. G. Thermophysical Properties of Fluid Systems. In: *NIST Chemistry WebBook, NIST Standard Reference Database Number 69*; Linstrom, P. J., Mallard, W. G., Eds.; National Institute of Standards and Technology: Gaithersburg, MD, June 2005, <http://webbook.nist.gov>.
- Ilmehls, E. C.; Gmehlung, J. *Ind. Eng. Chem. Res.* **2001**, *40*, 4470.
- Comuñas, M. J. P.; Baylaucq, A.; Boned, C.; Fernández, J. *Int. J. Thermophys.* **2001**, *22*, 749.
- Alcalde, R.; Aparicio, S.; García, B.; Dávila, M. J.; Leal, J. M. *New J. Chem.* **2005**, *29*, 817.
- Cerdeirinha, C. A.; Mínguez, J. A.; Carballo, E.; Tovar, C. A.; de la Puente, E.; Romaní, L. *Thermochim. Acta* **2000**, *347*, 37.
- Zabransky, M.; Ruzicka, V.; Mayer, V.; Domalski, E. S. *J. Phys. Chem. Ref. Data (Monograph No. 6) Heat Capacities of Liquids. Critical Review and Recommended Values*. ACS and AIP for NIST, **1996**.
- Frisch, M. J.; Trucks, G. W.; Schlegel, H. B.; Scuseria, G. E.; Robb, M. A.; Cheeseman, J. R.; Montgomery, Jr., J. A.; Vreven, T.; Kudin, K. N.; Burant, J. C.; Millam, J. M.; Iyengar, S. S.; Tomasi, J.; Barone, V.; Mennucci, B.; Cossi, M.; Scalmani, G.; Rega, N.; Petersson, G. A.; Nakatsuji, H.; Hada, M.; Ehara, M.; Toyota, K.; Fukuda, R.; Hasegawa, J.; Ishida, M.; Nakajima, T.; Honda, Y.; Kitao, O.; Nakai, H.; Klene, M.; Li, X.; Knox, J. E.; Hratchian, H. P.; Cross, J. B.; Adamo, C.; Jaramillo, J.; Gomperts, R.; Stratmann, R. E.; Yazyev, O.; Austin, A. J.; Cammi, R.; Pomelli, C.; Ochterski, J. W.; Ayala, P. Y.; Morokuma, K.; Voth, G. A.; Salvador, P.; Dannenberg, J. J.; Zakrzewski, V. G.; Dapprich, S.; Daniels, A. D.; Strain, M. C.; Farkas, O.; Malick, D. K.; Rabuck, A. D.; Raghavachari, K.; Foresman, J. B.; Ortiz, J. V.; Cui, Q.; Baboul, A. G.; Clifford, S.; Cioslowski, J.; Stefanov, B. B.; Liu, G.; Liashenko, A.; Piskorz, P.; Komaromi, I.; Martin, R. L.; Fox, D. J.; Keith, T.; Al-Laham, M. A.; Peng, C. Y.; Nanayakkara, A.; Challacombe, M.; Gill, P. M. W.; Johnson, B.; Chen, W.; Wong, M. W.; Gonzalez, C.; Pople, J. A. *Gaussian 03*, revision C.02; Gaussian, Inc.: Wallingford, CT, 2004.
- Becke, A. D. *Phys. Rev. A* **1988**, *38*, 3098.
- Lee, C.; Yang, W.; Parr, R. G. *Phys. Rev. B* **1988**, *37*, 785.
- Becke, A. D. *J. Chem. Phys.* **1993**, *98*, 5648.
- Singh, U. C.; Kollman, P. A. *J. Comput. Chem.* **1984**, *5*, 129.
- Besler, B. H.; Merz, K. M.; Kollman, P. A. *J. Comput. Chem.* **1990**, *11*, 431.
- Simon, S.; Duran, M.; Dannenberg, J. J. *J. Chem. Phys.* **1996**, *105*, 11024.

- (43) Ponder, J. W. *TINKER: Software tool for molecular design*, 4.2 ed.; Washington University School of Medicine: St. Louis, MO, 2004.
- (44) Hoover, W. G. *Phys. Rev. A* **1985**, *31*, 1695.
- (45) Allen, M. P.; Tildesley, D. J. *Computer Simulation of Liquids*; Clarendon Press: Oxford, UK, 1989.
- (46) Rickaert, J. P.; Cicotti, G.; Berendsen, H. J. *J. Comput. Phys.* **1977**, *23*, 327.
- (47) Essmann, U. L.; Perera, M. L.; Berkowitz, T.; Darden, H.; Lee, H.; Pedersen, L. G. *J. Chem. Phys.* **1995**, *103*, 8577.
- (48) (a) Martínez, J. M.; Martínez, L. *J. Comput. Chem.* **2003**, *24*, 819. (b) Friedlander, A.; Martínez, J. M.; Santos, S. A. *Appl. Math. Opt.* **1994**, *30*, 235.
- (49) Jorgensen, W. L.; Maxwell, D. S.; Tirado-Rives, J. *J. Am. Chem. Soc.* **1996**, *118*, 11225.
- (50) Palomar, J.; Ferro, V. R.; Gilarranz, M. A.; Rodríguez, J. *J. Phys. Chem. B* **2007**, *111*, 168.
- (51) Hunt, P. A.; Gould, I. R. *J. Phys. Chem. A* **2006**, *110*, 2269.
- (52) Hunt, P. A.; Kirchner, B.; Welton, T. *Chem.—Eur. J.* **2006**, *12*, 6762.
- (53) Yu, G.; Zhang, S.; Yao, X.; Zhang, J.; Dong, K.; Dai, W.; Mori, R. *Ind. Eng. Chem. Res.* **2006**, *45*, 2875.
- (54) Pereiro, A. B.; Santamarta, F.; Tojo, E.; Tojo, J. *J. Chem. Eng. Data* **2006**, *51*, 952.
- (55) Sanchez, I. C.; Lacombe, R. H. *Macromolecules* **1978**, *11*, 1145.
- (56) Kazarian, S.; Briscoe, B. J.; Welton, T. *Chem. Commun.* **2000**, 2047.
- (57) Rebelo, L. P. N.; Najdamovic, V.; Visak, Z. P.; Nunes da Ponte, M.; Szydłowski, J.; Cerdeirinha, C. A.; Troncoso, J.; Romaní, L.; Esperança, J. M. S. S.; Guedes, H. J. R.; Sousa, H. C. *Green Chem.* **2004**, *6*, 369.
- (58) Kumar, A. *J. Sol. Chem.* **2008**, *37*, 203.
- (59) Dack, M. R. J. *Chem. Soc. Rev.* **1975**, *4*, 211.
- (60) Woodcock, L. V.; Singer, K. *Trans. Faraday Soc.* **1971**, *67*, 12.
- (61) Ludwig, R.; Kragl, U. *Angew. Chem., Int. Ed.* **2007**, *46*, 6582.
- (62) Gomez de Azevedo, R.; Esperança, J. M. S. S.; Szydłowski, J.; Visak, Z. P.; Pires, P. F.; Guedes, H. J. R.; Rebelo, L. P. N. *J. Chem. Thermodyn.* **2005**, *37*, 888.
- (63) Strecham, A. A.; Paulechka, Y. U.; Kabo, A. G.; Blokhin, A. V.; Kabo, G. J. *J. Chem. Eng. Data* **2007**, *52*, 1791.
- (64) Fernández, A.; Torrecilla, J. S.; García, J.; Rodríguez, F. *J. Chem. Eng. Data* **2007**, *52*, 1979.
- (65) Zhang, Z.; Tan, Z.; Sun, L.; Zhen, Y.; Lv, X.; Shi, Q. *Thermochim. Acta* **2006**, *447*, 141.
- (66) Moens, L.; Blake, D. M.; Rudnicki, D. L.; Hale, M. J. *J. Sol. Energy Eng.* **2003**, *125*, 112.
- (67) Bowers, J.; Butts, C. P.; Martin, P. J.; Vergara, M. C. *Langmuir* **2004**, *20*, 2191.
- (68) Lee, S. U.; Jung, J.; Han, Y.-K. *Chem. Phys. Lett.* **2005**, *406*, 332.
- (69) (a) Zhang, Z. Z.; Chang, Z.; Xu, K.; Angell, C. A. *Electrochim. Acta* **2000**, *45*, 1229. (b) Tokuda, H.; Hayamizu, K.; Ishii, K.; Susan, M.; Watanabe, M. *J. Phys. Chem. B* **2005**, *109*, 6103.
- (70) Angell, C. A.; Bressel, R. D. *J. Phys. Chem.* **1978**, *82*, 2622.
- (71) (a) Xu, W.; Cooper, E. I.; Angell, C. A. *J. Phys. Chem. B* **2003**, *107*, 6170. (b) Xu, W.; Wang, L. M.; Nieman, R. A.; Angell, C. A. *J. Phys. Chem. B* **2003**, *107*, 11749.
- (72) Ingram, J. A.; Moog, R. S.; Ito, N.; Biswas, R.; Maroncelli, M. J. *Phys. Chem. B* **2003**, *107*, 5926.
- (73) Fraser, K. J.; Izgorodina, E. I.; Forsyth, M.; Scott, J. L.; MacFarlane, D. R. *Chem. Commun.* **2007**, 3817.
- (74) (a) Shah, J. K.; Brennecke, J. F.; Maginn, E. J. *Green Chem.* **2002**, *4*, 112. (b) Shah, K. K.; Maginn, E. J. *Fluid Phase Equilib.* **2004**, *222*–223, 195.
- (75) Canongia, J. N.; Padua, A. A. H.; Shimizu, K. *J. Phys. Chem. B* **2008**, *112*, 5039.
- (76) Liu, Z.; Huang, S.; Wang, W. *J. Phys. Chem. B* **2004**, *108*, 12978.
- (77) Armstrong, J. P.; Hunt, C.; Jones, R. G.; Licence, P.; Lovelock, K. R. J.; Satterley, C. J.; Villar-Garc, I. *J. Phys. Chem. Chem. Phys.* **2007**, *9*, 982.
- (78) Köddermann, T.; Paschek, D.; Ludwig, R. *ChemPhysChem* **2008**, *9*, 549.
- (79) Morrow, T. I.; Maginn, E. J. *J. Phys. Chem. B* **2002**, *106*, 12807.
- (80) Swiderski, K.; McLean, A.; Gordon, C. M.; Vaughan, D. H. *Chem. Commun.* **2004**, 2178.
- (81) Jin, H.; O'Hare, B.; Dong, J.; Arzhantsev, S.; Baker, G. A.; Wishart, J. F.; Benesi, A. J.; Maroncelli, M. *J. Phys. Chem. B* **2008**, *112*, 81.
- (82) Margulis, C.; Stern, H. A.; Berne, B. J. *J. Phys. Chem. B* **2002**, *106*, 12017.

JP9003467